nature communications

Article https://doi.org/10.1038/s41467-024-50578-5

Cycling and persistence of iron-bound organic carbon in subseafloor sediments

Received: 3 September 2023

Accepted: 16 July 2024

Published online: 29 July 2024

Check for updates

Yunru Chen[1,2], Liang Dong[3], Weikang Sui[3], Mingyang Niu[1], Xingqian Cui[3], Kai-Uwe Hinrichs[2,4] & Fengping Wang[1,3,5]

Reactive iron (Fe_R) serves as an important sink of organic carbon (OC) in marine surface sediments, which preserves approximately 20% of total OC (TOC) as reactive iron-bound OC (Fe_R-OC). However, the fate of Fe_R-OC in subseafloor sediments and its availability to microorganisms, remain undetermined. Here, we reconstructed continuous Fe_R-OC records in two sediment cores of the northern South China Sea encompassing the suboxic to methanic biogeochemical zones and reaching a maximum age of ~100 kyr. The down-core Fe_R-OC contributes a relatively stable proportion of 13.3 ± 3.2% to TOC. However, distinctly lower values of less than 5% of TOC, accompanied by notable ^{13}C depletion of Fe_R-OC, are observed in the sulfate-methane transition zone (SMTZ). Fe_R-OC is suggested to be remobilized by microbially mediated reductive dissolution of Fe_R and subsequently remineralized, the flux of which is 18–30% of the methane consumption in the SMTZ. The global reservoir of Fe_R-OC in microbially active Quaternary marine sediments could be 19-46 times the size of the atmospheric carbon pool. Thus, the Fe_R-OC pool may support subseafloor microorganisms and contribute to regulating Earth's carbon cycle.

On geological timescales, the burial rate of sedimentary organic carbon (OC) exerts major control on the concentrations of atmospheric O_2 and CO_2[1] and thus substantially influences Earth's environmental conditions. Reactive iron (Fe_R, defined as iron (oxyhydr)oxides that can be reductively dissolved by sodium dithionite) can promote the preservation of OC in a wide range of terrestrial and marine environments[2–6], as reactive iron-bound OC (Fe_R-OC) has long been believed to be more resistant to microbial degradation under aerobic conditions[7,8]. It is estimated that ~20.2 ± 15.5% of the total OC (TOC) is directly bound to Fe_R in marine surface sediments[9], which corresponds to a global reservoir of 7–54 Pg of OC (roughly 1–6% of the amount of the atmospheric CO_2)[9,10], demonstrating its potentially important role in preserving the sedimentary OC. A comprehensive picture regarding the fate of Fe_R-OC on geological timescales is still lacking but several studies of sediments of Pleistocene as well as late Paleocene to early Eocene age suggest that the fraction of Fe_R-OC in TOC (fFe_R-OC) remains relatively stable[11–14]. However, the question to what degree the Fe_R-OC reservoir interacts with sedimentary biogeochemical processes, in particular those involving redox reactions of iron and sulfur, remains unresolved.

Fe_R has long been found to promote organic matter preservation in terrestrial soils as well, especially via adsorption[5,15]. However, recent studies indicated the interactions between Fe_R and OC in soils are highly influenced by the redox oscillations during water-table fluctuations[16–18] in terrestrial environments. Under anoxic conditions, Fe_R reduction releases Fe_R-OC and increases the anaerobic remineralization of soil organic matter[17,18]. While under oxic conditions, newly-formed Fe_R promotes OC retention on mineral surfaces[16].

[1]State Key Laboratory of Microbial Metabolism, School of Life Sciences and Biotechnology, Shanghai Jiao Tong University, Shanghai 200240, China. [2]MARUM-Center for Marine Environmental Sciences, University of Bremen, D-28359 Bremen, Germany. [3]Key Laboratory of Polar Ecosystem and Climate Change, Ministry of Education, and School of Oceanography, Shanghai Jiao Tong University, Shanghai 200240, China. [4]Faculty of Geosciences, University of Bremen, D-28359 Bremen, Germany. [5]Southern Marine Science and Engineering Guangdong Laboratory (Zhuhai), Zhuhai 519000, China.
e-mail: fengpingw@sjtu.edu.cn

 https://doi.org/10.1038/s41467-024-50578-5

In anoxic marine sediments, Fe_R is one electron acceptor actively involved in biogeochemical processes[19–21]. Both Fe_R reduction by microorganisms and biogenic sulfide produced during sulfate reduction could potentially weaken the association with OC. Indeed, recent lab incubations demonstrated that Fe_R-OC can be remobilized during microbial iron reduction and subsequently utilized as an electron donor and/or carbon source for microbial communities[22–24]. Consequently, the remobilization of Fe_R-OC during early diagenesis may influence the relative size of the Fe_R-OC reservoir that is preserved in sediments for a long time. Additionally, the supply of Fe_R-OC is expected to depend on the hydrological conditions through the influence on continental weathering and Fe_R formation as well as on sea level through the influence on shelf topography and thus the transport of continental detritus into the deep sea[25–27]; both factors are expected to vary periodically on glacial-interglacial timescales. To disentangle the effect of Fe_R-OC supply and early diagenetic reworking on sedimentary Fe_R-OC, downcore Fe_R-OC records need to be established and related to both geochemical zonation and sediment chronology.

In this study, we analyzed two gravity cores (QDN-G1 and QDN-14B, Fig. 1a) from the northern South China Sea in order to determine the fate of the sedimentary Fe_R-OC via its quantitative and isotopic analysis. The core QDN-G1 represents typical continental slope sediments (1478 m water depth), while core QDN-14B (1370 m water depth), around 35 km southwest from core QDN-G1, was influenced by nearby cold seeps expelling methane-rich fluids[28]. Consequently, QDN-14B can be used to comparatively evaluate the influence of microbial activities on the potential remobilization of Fe_R-OC in the diagenetically active zones where sulfate reduction coupled to either organic matter remineralization or methane oxidation occurs. Meanwhile, the core QDN-G1 consisting of sediments with relatively low microbial activity is used for exploring the long-term preservation of Fe_R-OC on glacial-interglacial timescale with well established age model covering the past 97 kyr (see Methods and Supplementary Fig. 1 for detailed information).

To quantify the amount of Fe_R-OC, the citrate-bicarbonate-dithionite (CBD) method described in detail by Lalonde et al.[2] and Salvadó et al.[3] was applied in this study (see Methods). This method targets only reactive iron (oxyhydr)oxides, which are presumably accessible for microorganisms, and leaves unreactive phases such as iron-containing silicates untouched[29]. By incorporating analyses of porewater geochemistry, including the concentrations of ferrous iron, sulfate, dissolved inorganic carbon (DIC), and the carbon isotope ratio of DIC ($\delta^{13}C_{DIC}$), all of which are tied to microbially mediated processes, our study takes a critical step in assessing the stability of sedimentary Fe_R-OC in response to post-depositional microbial activities and sheds lights on its fate in subseafloor sediments.

Results and discussion

Fe_R-OC remobilization in SMTZ sediments

The core recoveries of QDN-G1 and QDN-14B were 10.8 m and 8.4 m, respectively. These two cores penetrated sediments with distinct diagenetic activities. Microbially mediated early diagenetic redox reactions have resulted in distinct geochemical zonation[30], i.e., the iron reduction zone (IRZ), the sulfate reduction zone (SRZ), the sulfate-methane transition zone (SMTZ), and the methanogenic zone (MZ) (Fig. 1b). Despite similar TOC contents in sediments from the two cores (see below), the higher methane fluxes and the associated rapid depletion of sulfate via anaerobic oxidation of methane resulted in a shallower SMTZ in core QDN-14B (280–440 cmbsf) compared to core QDN-G1 (potentially around 720–960 cmbsf) (Fig. 1b). This difference in activity is supported by geochemical modeling (see Methods), which showed a more than two times higher net sulfate reduction rate in the SMTZ in core QDN-14B compared to core QDN-G1 (0.034 vs. 0.015 mol m^{-3} yr^{-1}) (Supplementary Fig. 4).

The Fe_R contents in the two cores range from 0.7 to 5.7 mg g^{-1}, which reaches the maximum at 200 cmbsf and 240 cmbsf in QDN-G1 and QDN-14B, respectively (Fig. 2a, f). TOC contents in the two cores range from 0.5 to 1.2% (Fig. 2b, g, black lines). The Fe_R-OC contents in the two cores range from 0.02 to 0.17% (Fig. 2b, g, red lines) and account for 3.2–20.5% of TOC (Fig. 2d, i). The downcore patterns of both TOC and Fe_R-OC content profiles are not consistent with that of Fe_R content. The presence of low levels of dissolved Fe(II) throughout the core QDN-G1 (3–35 µM, Fig. 1b) is consistent with some background activity of dissimilatory iron reduction, independent of the biogeochemical zone. However, there is no discernable imprint on the content of Fe_R-OC, except in the SMTZ (Fig. 2b). Interestingly, both the lowest Fe_R-OC content and the lowest fFe_R-OC occurred in the SMTZ of each core. In QDN-G1 and QDN-14B, the average Fe_R-OC contents in non-SMTZ sediments are 0.12% and 0.10%, respectively, but drop to

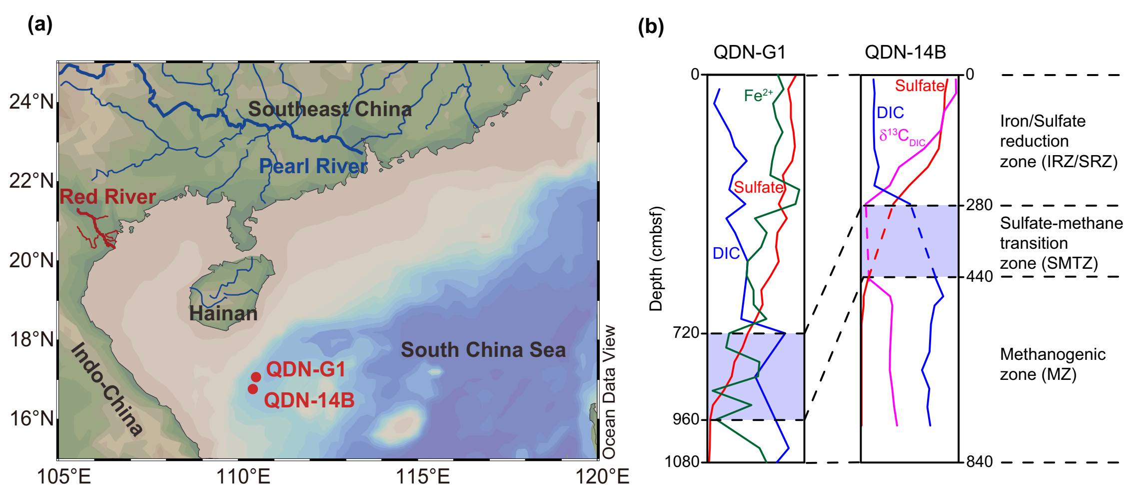

Fig. 1 | Map of the cores studied in the northern South China Sea and their biogeochemical zonation. a Map of cores QDN-G1 and QDN-14B. River systems entering the northern South China Sea are indicated by blue and red lines. **b** A schematic of biogeochemical zonation, including iron reduction zone (IRZ), sulfate reduction zone (SRZ), sulfate-methane transition zone (SMTZ) and methanogenic zone (MZ), in cores QDN-G1 and QDN-14B inferred by porewater geochemistry. Fe(II) concentration, sulfate concentration, dissolved inorganic carbon (DIC) concentration and carbon isotope ratio of DIC ($\delta^{13}C_{DIC}$) are shown in green, red, blue and magenta lines, respectively. The location of the SMTZ is highlighted in purple. Porewater geochemistry data in QDN-14B are from Niu et al., 2017 and Hu et al., 2019[28,60]. Detailed porewater geochemistry data are plotted in Supplementary Fig. 2 and 3. Source data are provided as a Source Data file.

https://doi.org/10.1038/s41467-024-50578-5

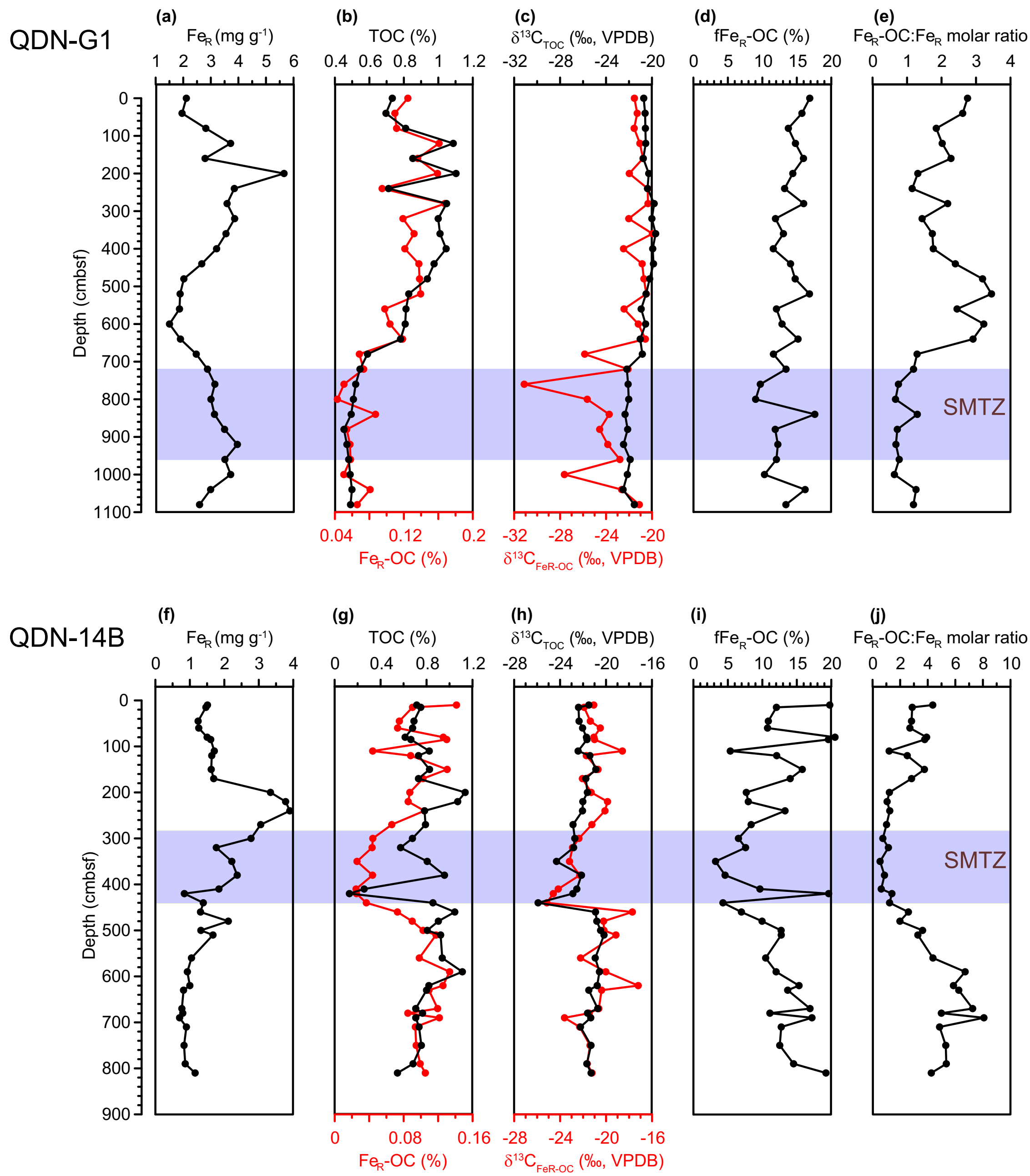

Fig. 2 | Content and $\delta^{13}C$ profiles of total organic carbon (TOC) and reactive iron-bound organic carbon (Fe_R-OC) in cores QDN-G1 (a–e) and QDN-14B (f–j). **a**, **f** Content of Fe_R. **b**, **g** Content of TOC (black lines) and Fe_R-OC (red lines). Separate x-axes are used for TOC and Fe_R-OC, labeled in the same color as the data profile. **c**, **h** Carbon isotope ratio of TOC (black lines) and Fe_R-OC (red lines). Separate x-axes are used for TOC and Fe_R-OC, labeled in the same color as the data profile. **d**, **i** The fraction of Fe_R-OC in TOC (fFe_R-OC). **e**, **j** The molar ratio of Fe_R-OC and Fe_R. The locations of the SMTZ are highlighted by the purple bars. Source data are provided as a Source Data file.

0.06% and 0.03% in the SMTZ sediments, respectively (Table 1). Similarly, the average fFe_R-OC in the non-SMTZ layers are 14.0% and 13.0%, repectively, but drop to 12.3% and 5.2% in the SMTZ sediments, respectively (Table 1).

The carbon isotope ratios of TOC ($\delta^{13}C_{TOC}$) and Fe_R-OC ($\delta^{13}C_{FeR\text{-}OC}$) provide insights into the sources of the corresponding OC pool. In QDN-G1 and QDN-14B, $\delta^{13}C_{TOC}$ varies from −22.5 to −19.7‰, and from −25.9 to −20.2‰, respectively (Fig. 2c, h, black lines); $\delta^{13}C_{FeR\text{-}OC}$ varies from −31.1 to −20.0‰, and from −25.2 to −17.2‰, respectively (Fig. 2c, h, red lines). Lower $\delta^{13}C_{TOC}$ and $\delta^{13}C_{FeR\text{-}OC}$ values are observed in SMTZ of both cores (Fig. 2c, h). The average $\delta^{13}C_{TOC}$ values of non-SMTZ sediments are −20.6 ± 0.7‰ and −21.5 ± 0.7‰, but 1.5‰ and 1.9‰ lower in SMTZ sediments in QDN-G1 and QDN-14B, respectively (Table 1). Similarly, the average $\delta^{13}C_{FeR\text{-}OC}$ values of non-SMTZ sediments are −21.8 ± 1.8‰ and −20.8 ± 1.4‰, but 3.1‰ and 2.8‰ lower in SMTZ sediments in QDN-G1 and QDN-14B, respectively (Table 1). All the $\delta^{13}C_{TOC}$ and $\delta^{13}C_{FeR\text{-}OC}$ values in non-SMTZ sediments indicate the accumulation of mainly marine-algal OC, which in the sampled area has an average $\delta^{13}C$ value of −20.8 ± 0.4‰[31]. However, terrestrial OC has much higher contribution in SMTZ sediments, where particulate terrestrial OC and riverine primary production have characteristic carbon isotope signatures of −24.1 ± 1.0‰ and −30.0 ± 2.6‰[32].

The cumulative evidence of lower Fe_R-OC content, lower fFe_R-OC, and lower $\delta^{13}C_{FeR\text{-}OC}$ in SMTZ sediments, compared to relatively uniform records in non-SMTZ sediments (significance levels in Table 1, see Methods for more information) is suggestive of dynamic organic

https://doi.org/10.1038/s41467-024-50578-5

Table 1 | Comparisons of the contents and carbon isotope ratios of TOC and Fe_R-OC between non-SMTZ and SMTZ sediments in two cores

QDN-G1	TOC (%)	Fe_R-OC (%)	fFe_R-OC (%)	$\delta^{13}C_{TOC}$ (‰, VPDB)	$\delta^{13}C_{FeR\text{-}OC}$ (‰, VPDB)
Non-SMTZ[a] (*n* = 21)	0.8 ± 0.2	0.12 ± 0.03	14.0 ± 1.9	−20.6 ± 0.7	−21.8 ± 1.8
SMTZ[a] (*n* = 7)	0.5 ± 0.0	0.06 ± 0.02	12.3 ± 2.8	−22.2 ± 0.2	−24.8 ± 3.0
Offset between non-SMTZ and SMTZ sediments[b]	0.3	0.06	1.8	1.5	3.1
P value	*P* = 3.1e−04	*P* = 3.1e−04	*P* = 0.1	*P* = 3.1e−04	*P* = 9.5e−04
QDN-14B	**TOC (%)**	**Fe_R-OC (%)**	**fFe_R-OC[c] (%)**	**$\delta^{13}C_{TOC}$ (‰, VPDB)**	**$\delta^{13}C_{FeR\text{-}OC}$ (‰, VPDB)**
Non-SMTZ[a] (*n* = 29)	0.8 ± 0.1	0.10 ± 0.02	13.0 ± 4.0	−21.5 ± 0.7	−20.8 ± 1.4
SMTZ[a](*n* = 7)	0.6 ± 0.3	0.03 ± 0.01	5.2 ± 1.8[c]	−23.3 ± 1.3	−23.5 ± 1.1
Offset between non-SMTZ and SMTZ sediments[b]	0.2	0.07	7.7	1.9	2.8
P value	*P* = 0.2	*P* = 4.8e−07	*P* = 5e−05	*P* = 1.6e−05	*P* = 7.1e−06

P values of the two-sided Wilcoxon rank sum test are shown. See Supplementary Fig. 5 for data visualized in box plots.
[a]Given are means±standard deviation.
[b]Offsets of corresponding averaged values between non-SMTZ and SMTZ sediments.
[c]fFe_R-OC data at 410 and 420 cmbsf in QDN-14B are biased by extremely low TOC and are not included for calculations (*n* = 5).

matter cycling in this sediment horizon. While we cannot entirely rule out that these distinct signals in SMTZs of both cores are related to the depositional history and coincidentally located in this horizon, we view this scenario as highly unlikely (see Supplementary Fig. 6 and Supplementary Discussion for details). Instead, we propose that the post-depositional microbial processes account for these distinctive characteristics of Fe_R-OC records.

Accordingly, two observations deserve attention: (i) the distinct depletions in ^{13}C content and contents of Fe_R-OC within the SMTZ, and (ii) sediments below the SMTZ show similar features with respect to ^{13}C content and contents of Fe_R-OC as sediments above the SMTZ. The relatively low content of Fe_R-OC strongly suggests that a substantial fraction of it has been remobilized and possibly remineralized. Two mechanisms could account for the low $\delta^{13}C_{FeR\text{-}OC}$ of the residual fraction: (a) remobilization/degradation of a ^{13}C-enriched, weakly bound and/or more reactive fraction[33] with the residual fraction being ^{13}C-depleted; since the $\delta^{13}C$ of the residual fraction is broadly consistent with an origin from terrestrial plants, the residual fraction could be tightly adsorbed terrestrial organic matter supplied together with the detrital minerals from land. (b) The alternative involves again remobilization of a large fraction of Fe_R-OC combined with adsorption of ^{13}C depleted dissolved organic matter (DOM) produced in the course of anaerobic oxidation of methane[34]; the extremely low molar ratios of Fe_R-OC to Fe_R below 1 in both SMTZs (Fig. 2e, j) indicate abundant binding sites available for DOM molecules[15,35]. These two mechanisms are not mutually exclusive and could act in combination. In any case, both scenarios require remobilization and possibly degradation of a substantial fraction of Fe_R-OC. The fact that sediments below the SMTZ resemble those above the SMTZ is at first surprising if we assume that the more deeply buried sediments were at some point in the geologic past also situated in the SMTZ. In this case, re-adsorption of DOM produced during cycling of particulate organic matter of marine origin could be the cause for the similarity of Fe_R-OC related signals above and below the SMTZ. However, there is also evidence that SMTZs do not "move" continuously through the sediment column with increasing sedimentation but rather "oscillate" from one horizon to another where they then remain stagnant in position for extended periods[36,37].

Remineralization of Fe_R-OC supports microorganisms in the SMTZ

The SMTZ as a discrete sedimentary horizon, where anaerobic oxidation of methane is coupled to sulfate reduction (S-AOM)[38], ubiquitously occurs in organic-rich continental shelf and slope sediments. S-AOM is performed syntrophically by sulfate-reducing bacteria and methanotrophic archaea[39]. In core QDN-14B, geochemical modeling reveals higher net sulfate reduction rates in the SMTZ stimulated by the methane-rich fluid in the core (Fig. 3b), which is further supported by the higher relative abundance and cell concentration of sulfate-reducing bacteria (Fig. 3e, f) and by elevated copy number of methyl-coenzyme M reductase subunit A (*mcrA*) gene (Fig. 3g)[28], the key marker gene for both methane-producing and methane-consuming archaea[40]. By contrast, in core QDN-G1, there is no evidence for elevated sulfate reduction activity in the SMTZ compared to the shallower sulfate reduction zone, based on modeled rates as well as relative and absolute abundance of sulfate-reducing bacteria (Supplementary Fig. 7b, e, f). This is consistent with the relatively moderate variation in fFe_R-OC record in core QDN-G1 compared to core QDN-14B. Collectively, these lines of evidence suggest that due to the particularly high methane flux at core QDN-14B, the microbial activity in the SMTZ has stimulated the remobilization of Fe_R-OC.

A plausible mechanism for Fe_R-OC remobilization in the SMTZ is the occurrence of reductive dissolution of Fe_R by the biogenic hydrogen sulfide produced during sulfate reduction[41,42], and subsequent release of Fe_R-OC. Apart from chemical reduction of Fe_R, sulfate-reducing bacteria may also reduce Fe_R directly[43], with the rate of reduction being enhanced by sulfate reduction and the presence of biogenic sulfide[44]. In addition, the process of AOM may be directly coupled with iron reduction (Fe-AOM)[45] and facilitate Fe_R dissolution in this zone. In summary, the reduction of Fe_R could be enhanced by biological and chemical processes in the SMTZ, and result in the remobilization of Fe_R-OC.

Assuming that both TOC as well as Fe_R-OC lost in the SMTZ are remineralized by heterotrophic microorganisms, the remineralization fluxes of TOC and Fe_R-OC in the SMTZ can be estimated by the difference of their average accumulation rates between the sediment column above and within the SMTZ (see methods). In QDN-14B, the SMTZ is well defined by the depletion of sulfate, increasing DIC, and low $\delta^{13}C_{DIC}$ values (Fig. 1b). The TOC and Fe_R-OC remineralization fluxes in the SMTZ are estimated to be 15.8 and 5.8 mol m^{-2} kyr^{-1}, respectively. Fe_R-OC remineralization contributes 36.7% to the TOC remineralization, which is disproportionally high compared to fFe_R-OC (5.2 ± 1.8%) in this zone. Therefore, Fe_R-OC is preferentially remineralized compared to OC that is not bound to Fe_R (non-Fe_R-OC) and results in the low fFe_R-OC. Stimulated by higher microbial activity, e.g., through S-AOM, Fe-AOM, and iron reduction, Fe_R-OC is remobilized and potentially remineralized in the SMTZ.

The estimation of the TOC and Fe_R-OC remineralization fluxes for core QDN-G1 is not as straightforward as for core QDN-14B due to the higher uncertainty of assigning the vertical extension of the SMTZ and the fact that contents of TOC and Fe_R-OC steadily decline already above the SMTZ within this core (Fig. 2b). This decline implies that in

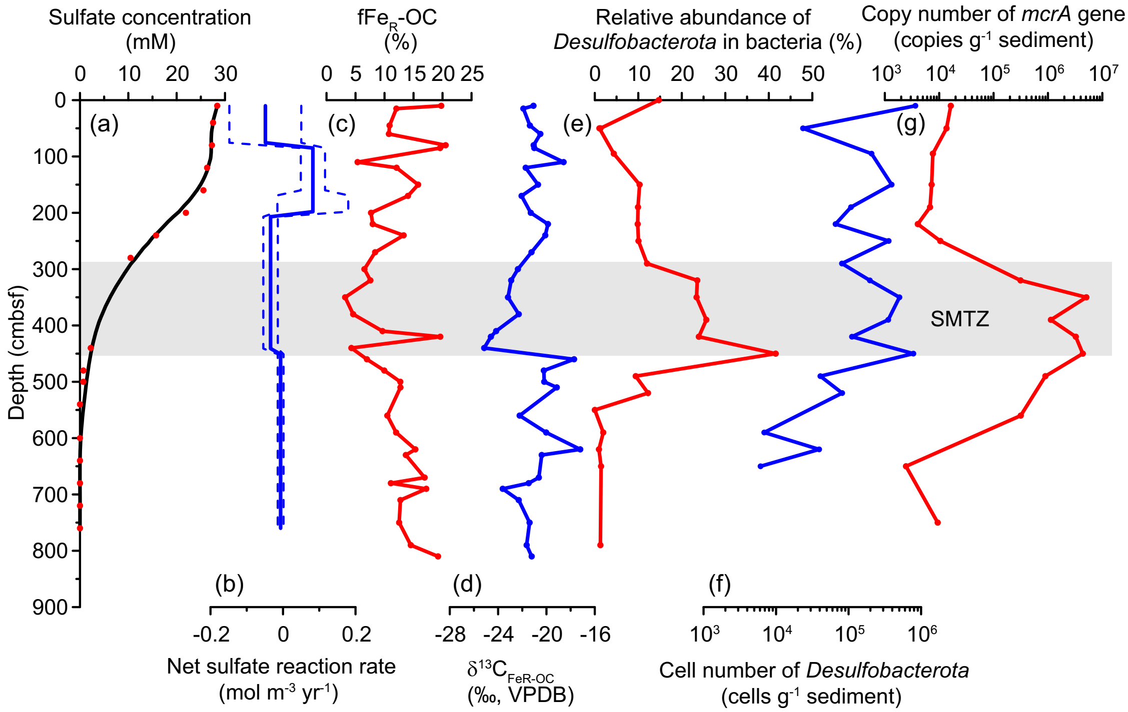

Fig. 3 | Geochemical modeling and microbial evidence show that a high sulfate reduction rate is associated with low fraction of Fe$_R$-OC in TOC (fFe$_R$-OC) in the SMTZ of QDN-14B. a Measured (red dots) and fitted (black line) sulfate concentrations. A 5-point Gaussian filter was applied to the concentration with the weighting on the 5 points of: [0.06, 0.24, 0.4, 0.24, 0.06][65]. The measured data are from Niu et al.[28] and Hu et al.[60]. **b** Modeled net reaction rate profile of sulfate. Negative values indicate net consumption, and positive values indicate net production. The 1σ envelope is shown in dashed line (See Methods for details). **c** Downcore record of fFe$_R$-OC. **d** Downcore record of $\delta^{13}C_{FeR\text{-}OC}$. **e** Relative abundance of *Desulfobacterota* in bacteria, to which most of the sulfate-reducing bacteria belong[78] (data from Niu et al.[28]). **f** The cell number of *Desulfobacterota*, translated from the cell number of bacteria by multiplying the relative abundance of *Desulfobacterota* in bacteria (data from Niu et al.[28]). **g** The copy number of *mcrA* gene (data from Niu et al.[28]). The gray bar shows the position of the SMTZ. Source data are provided as a Source Data file.

this core the remineralization fluxes are partially unrelated to processes within the SMTZ. To address this, we used an additional approach for estimating a lower flux boundary, which is only based on the four samples directly above the SMTZ as average (see methods). The resulting range of TOC and Fe$_R$-OC remineralization fluxes for core QDN-G1 are 21.6–32.8 mol m^{-2} kyr^{-1} and 3.3–5.0 mol m^{-2} kyr^{-1}, repectively. Fe$_R$-OC remineralization contributes 10.1–23.1% to the TOC remineralization, which is comparable to the fFe$_R$-OC (12.3 ± 2.6%) in this zone.

Altogether, the remineralization of Fe$_R$-OC may substantially contribute to TOC remineralization in the SMTZ. Moreover, since Fe$_R$-OC is likely enriched in labile organic matter[2], it has the potential to enhance the activity and growth of heterotrophic microbial communities in subseafloor sediments and be rapidly recycled upon remobilization. Considering that the SMTZ is ubiquitous in continental slope sediments[46], and assuming a Fe$_R$-OC remineralization flux of 3.3–5.8 mol m^{-2} kyr^{-1} as observed in the SMTZ of the two cores and a continental slope area of 3.01×10^7 km^2 [46], the global Fe$_R$-OC remineralization flux in the SMTZ of the continental slope area is estimated to be 0.10–0.17 Tmol yr^{-1}, which is about 18-30% of the methane consumption flux in the SMTZ of continental slope sediments (0.56 Tmol yr^{-1} [46]) and 0.61% of the global sedimentary OC burial rate (13.3 Tmol yr^{-1} [47]). Using acetate as a proxy for OC, and the Gibbs energies of OC oxidation by sulfate of −81.5 KJ (per mol acetate)[48] at 5 °C and 100 bars of pressure (1000 m water depth), the remineralization of Fe$_R$-OC in the SMTZ of the continental slope can provide a power supply from 4.1×10^{15} to 6.9×10^{15} J yr^{-1}. Assuming the cellular power demand for organisms oxidizing OC with sulfate of 7.7×10^{-14} W cell^{-1} [48], the Fe$_R$-OC remineralization in the SMTZ of continental slope area could sustain a biomass from 1.7×10^{21} to 2.8×10^{21} microbial cells. Considering generally lower power demand of 10^{-20} to 10^{-16} W cell^{-1} for microorganisms in marine sediments[49], this amount of energy could potentially support an even larger population from 1.3×10^{24} to 2.2×10^{28} microbial cells. The average SMTZ depth in continental slope sediments is estimated to be 12.8 ± 12.1 m below seafloor[46], where the cell abundance typically ranges from 10^6 to 10^8 cells cm^{-3} [50]. Assuming the SMTZ depth interval of 1 m, the volume of global continental slope SMTZ sediments reaches 3×10^{13} m^3, which harbors from 3×10^{25} to 3×10^{27} cells. Therefore, the remineralization of Fe$_R$-OC in continental slope SMTZ sediments could support a substantial fraction of subseafloor microbial life in this zone.

Fe$_R$ as an important reservoir of labile OC in marine sediments

The seafloor receives Fe$_R$ mainly from terrestrial input[27,51], which is typically associated with terrestrial OC[52–54]. After entering the ocean, additional organic matter from the pool of marine dissolved organic carbon may be bound to Fe$_R$-bearing minerals by adsorption[55,56]. Finally, after deposition in sediments, the upward diffusing Fe(II) can coprecipitate with marine OC into authigenic Fe$_R$ after re-oxidation at the redox interface[57]. The binding mechanism between Fe$_R$ and OC in marine sediments has been inferred from the molar ratio of Fe$_R$-OC to Fe$_R$[2], with adsorption and coprecipitation characterized by ratios of <1 and 6–10, respectively[2,15]. In the two cores studied here, the molar ratio of Fe$_R$-OC to Fe$_R$ is always larger than 1, except in the SMTZ, suggestive of a mixed binding mechanism of adsorption and coprecipitation (Fig. 2e, j). Furthermore, $\delta^{13}C_{FeR\text{-}OC}$ values in both sediment cores are typical for marine-sourced OC and the high molar ratio of Fe$_R$-OC to Fe$_R$ indicates coprecipitation as an important binding mechanism. All these clues suggest that a major proportion of Fe$_R$-OC in marine sediments is intrinsically labile marine OC.

https://doi.org/10.1038/s41467-024-50578-5

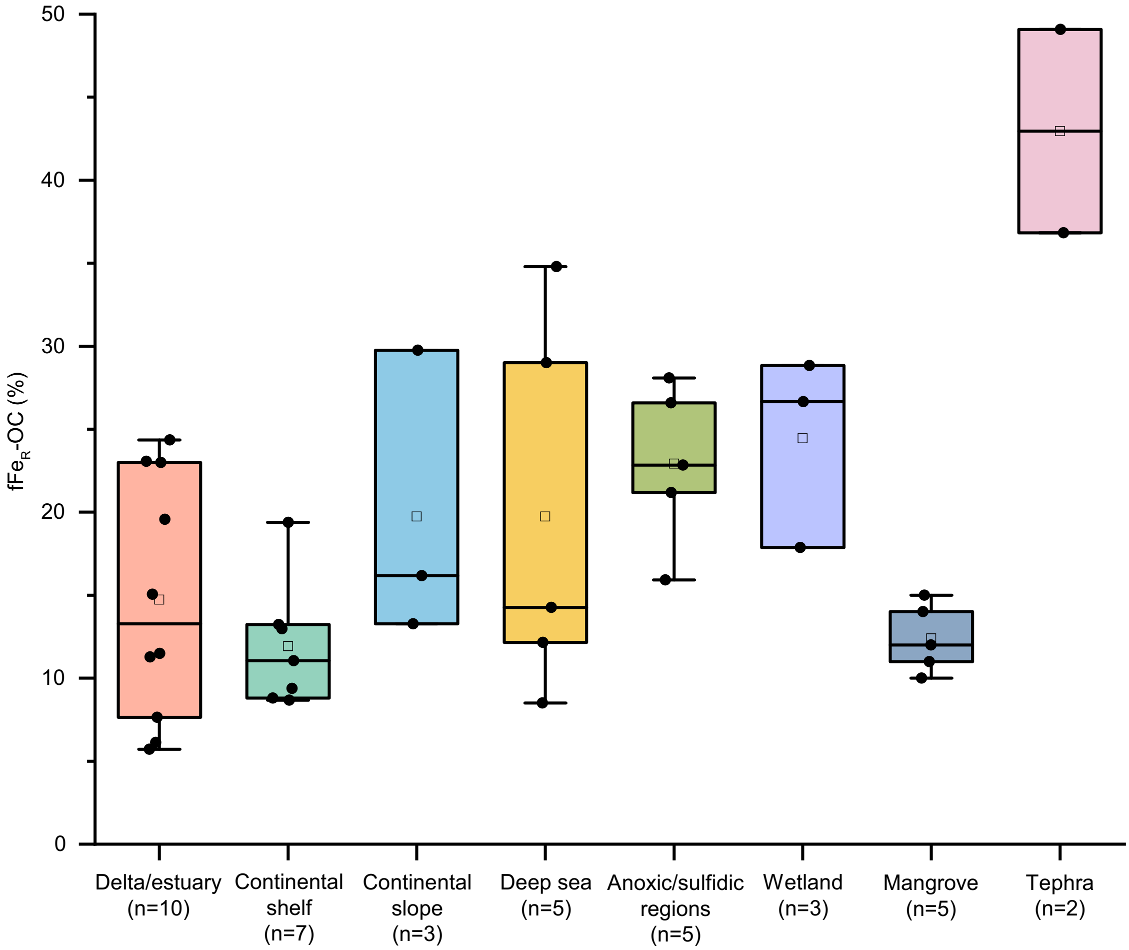

Fig. 4 | Fraction of Fe_R-OC in TOC (fFe_R-OC) values of surface sediments in different marine environments. All the published fFe_R-OC data obtained from marine sediments using the CBD method were compiled (detailed information of data cited are listed in Supplementary Table 3). The average fFe_R-OC value of each study area was calculated to avoid overrepresentation of study areas with large numbers of data points (Supplementary Table 3). The average fFe_R-OC values were then grouped into eight categories according to the depositonal environments of these study areas and used for statistical analyzes and box-whisker plots. Box plots indicate mean (open square), median (middle line), 25th, 75th percentile (box) and 1.5 times interquartile range (whiskers) with data points (solid dots) overlapped on top. The outlier ($n = 1$) in the mangrove group is not shown. Source data are provided as a Source Data file.

The average fFe_R-OC in the two cores studied, except within the SMTZ in QDN-14B, is 13.3 ± 3.2%. The relatively stable fFe_R-OC in the two cores suggests a similar degradation rate of Fe_R-OC and non-Fe_R-OC on the timescales represented by these cores. The only exception is the active SMTZ in QDN-14B, where iron reduction is enhanced significantly by processes likely induced by sulfate-reducing bacteria, methanotrophic archaea and/or biogenic sulfide. The stimulated degradation of Fe_R-OC over non-Fe_R-OC leads to extremely low fFe_R-OC in the SMTZ of QDN-14B. As these especially active SMTZs have limited distribution in global marine sediments and occupy narrow depth intervals in sediment columns, the overall impact on the Fe_R-OC reservoir in subseafloor sediments is small.

Taken together, the Fe_R-OC records in these two cores suggest that a stable proportion of TOC survives early diagenesis as Fe_R-OC and is sequestered in marine sediments on at least 100-kyr timescales. Considering previous studies showing high fFe_R-OC in the samples even from late Paleocene to early Eocene[12], persistence of Fe_R-OC on even longer timescale is expected in marine sediments. This enables a rough estimation of the global Fe_R-OC reservoir by multiplying the TOC reservoir in global marine sediments from the Quaternary Period (0–2.59 Ma) storage[48] with published fFe_R-OC data in marine surface sediments. For deriving representative fFe_R-OC values, all published fFe_R-OC data in marine sediments using the CBD method were compiled and combined with our measured data and grouped into eight categories based on their study area information: delta and estuary, continental shelf, continental slope, deep sea, anoxic/sulfidic regions, wetland, mangrove and tephra (Fig. 4, Supplementary Table 3). One-way ANOVA and Tukey Honest Significant Difference (HSD) test revealed that significant difference ($P < 0.05$) in fFe_R-OC values exists only between tephra-containing sediments and other environments (Supplementary Table 4). Considering TOC storage in the Quaternary sediments is estimated in the three domains shelf (water depth < 200 m), margin (200 m <water depth < 3500 m) and abyss (water depth > 3500 m)[48], delta/estuary and continental shelf were combined to represent shelf, continental slope was used to represent margin and deep sea was used to represent abyss. Combining the published TOC reservoir and the corresponding surface fFe_R-OC values in these three domains[48], the global Fe_R-OC reservoir in Quaternary marine sediments was estimated to be 28,690 ± 12,165 Pg C (Supplementary Table 5), which is approximately 19–46 times the size of the atmospheric carbon pool.

Methods

Sediment core collection and age model establishment

The Qiongdongnan (QDN) basin lies in the rift belt of the northern continental margin of the South China Sea and receives terrestrial material mainly from the Indo-China Peninsula and Southeast China (especially Hainan Island) by river runoff and eolian dust[58,59].

In addition, the material contribution of marine authigenic sources to the basin cannot be neglected[59].

Core QDN-14B was recovered from the QDN basin at a water depth of 1370 m in 2015, ~600 m east of ROV1, which is an active seep site of "Haima" cold seeps[60]. Core QDN-G1 was recovered outside the area of "Haima" cold seeps around 35 km away from QDN-14B at a water depth of 1478 m in 2018 (Fig. 1a). Sediment samples in core QDN-G1 were subsampled every 40 cm and preserved at −80 °C. Known volumes of sediments were taken using tip cut-off syringes and sealed in glass vials for further measurements of density and porosity. For core QDN-G1, the age model of the upper 4.0 m was based on 7 accelerator mass spectrometry ^{14}C ages of planktonic foraminifera (*G. ruber*) performed at the Beta Analytic Laboratory (Florida, USA) (Supplementary Table 1). The age model of the lower part (4.0–10.8 m) was established by aligning the benthic foraminifera (*C.wuellerstorfi*) δ^{18}O record to the global benthic δ^{18}O stack LR04[61] using the software QAnalySeries (v. 1.4.2) (Supplementary Fig. 1).

Porewater sampling and analysis

Porewater samples were extracted immediately onboard using Rhizon samplers (0.22 µm filter) before the core was cut open for sediment subsampling. To prevent oxidation of Fe(II), an aliquot of porewater was added to the ferrozine solution. Porewater samples for DIC measurements were preserved in pre-vacuumed glass vials. Porewater samples for ion measurements were acidified with concentrated HNO_3. The rest of the porewater samples were preserved in pre-combusted amber glass vials at −20 °C for dissolved organic carbon measurements.

The Fe(II) concentration was determined by ferrozine assay[62] using a spectrophotometer (DR5000, Hach, USA). The concentrations of major cations and anions were determined by ion chromatography (Dionex ICS-5000 + , Thermo Scientific, USA). Dissolved inorganic carbon (DIC) was measured using a total carbon analyzer (Multi 3100, Analytik Jena, Germany).

Physical properties of bulk sediments

Known volumes of sediments were subsampled by tip cut-off syringes and preserved in sealed glass vials for the measurements of physical properties, such as porosity and dry bulk density. All the physical properties were only measured for QDN-G1 samples. The averaged porosity and dry bulk density were used to represent the general porosities of the two cores.

Porosity was calculated by the volume ratio of water and wet sediment, where the volume of water was calculated from the difference between the wet and dry sample weight. The dry bulk density was calculated by dividing the dry sample weight by the original wet sample volume.

Fe_R and Fe_R-OC extraction

Fe_R and Fe_R-OC were extracted using the citrate-bicarbonate-dithionite (CBD) method according to Mehra and Jackson (1960)[29], as modified by Lalonde et al.[2] and Salvadó et al.[3]. Both poorly crystalline and crystalline iron (oxyhydr)oxides can be reduced by this method, including mainly goethite and hematite, which are the major iron (oxyhydr)oxides in marine sediments[63,64]. Briefly, samples were freeze-dried and homogenized using an agate mortar and pestle. Samples (0.5 g) were weighed carefully into 40 mL Teflon tubes and extracted in a 30 mL solution of sodium dithionite (Cat. No. 71699-50 G, Sigma-Aldrich, Germany) and trisodium citrate (Cat. No.1009408, Sinopharm, China) buffered with sodium bicarbonate (Cat. No. S837271-500G, Macklin, China) at 80 °C for 15 min in a water bath. After the extraction, the suspensions were centrifuged for 10 min at 4000 × g and then rinsed 5 times with artificial seawater. To evaluate the amount of OC remobilized during the extraction that was not bound to Fe_R, another sample aliquot was extracted as a control under the same experimental conditions, but replacing sodium dithionite and trisodium citrate with sodium chloride (Cat. No. 10019308, Sinopharm, China) with equivalent ion strength. The residuals were dried overnight in a 50 °C oven, carefully weighed and manually ground.

The supernatant and rinse water were combined, acidified to pH < 2 and filtered through 0.22 µm filters. The dissolved iron was determined using a ferrozine assay[62]. The iron extracted in the control group were negligible; therefore, the amount of Fe_R was calculated based on the iron extracted in the dithionite reduction group without further correction.

Fe_R-OC quantification and carbon isotope analyzes

The OC content and carbon isotope ratio were determined for both untreated and treated samples using an elemental analyzer (Vario EL III, Elementar) coupled to an isotope ratio mass spectrometer (Isoprime, Elementar) at the instrumental analysis centre, Shanghai Jiao Tong University. The inorganic carbon was removed by acid fumigation before the analysis. The samples were measured in triplicate, and the standard deviation was <0.05% for TOC and <0.2‰ for δ^{13}C. The analytical precision was <0.06% for TOC (standard deviation for repeated measurements of the low organic content soil standard; $n = 3$) and <0.09‰ for δ^{13}C (standard deviation for repeated measurements of the USGS40 standard, $n = 3$).

Calculation of fFe_R-OC and $\delta^{13}C_{FeR\text{-}OC}$

The fraction of Fe_R-OC in TOC (fFe_R-OC) was determined as the difference of TOC amount in the residuals between the CBD extraction and control extraction devided by the TOC amount in the untreated sample.

$$fFe_R\text{-}OC = (TOC_{control}\text{-}TOC_{CBD})/TOC_{bulk} \tag{1}$$

in which,

$TOC_{control}$ = total organic carbon (mg) left after the control extraction,

TOC_{CBD} = total organic carbon (mg) left after the CBD extraction,

TOC_{bulk} = total organic carbon (mg) in the untreated sample.

A binary mixing model was used to calculate the carbon isotope ratio of Fe_R-OC, where the OC pool in the residual of the control group ($TOC_{control}$) is comprised of Fe_R-OC and OC remaining untouched after CBD extraction (TOC_{CBD}). The carbon isotope ratios of Fe_R-OC was calculated according to the following mass-balanced equations:

$$TOC_{CBD} + Fe_R\text{-}OC = TOC_{control} \tag{2}$$

$$f TOC_{CBD} \times \delta^{13}C_{CBD} + f Fe_R\text{-}OC \times \delta^{13}C_{FeR\text{-}OC} = \delta^{13}C_{control} \tag{3}$$

in which,

Fe_R-OC = the amount of organic carbon (mg) bound to Fe_R,

TOC_{CBD} = total organic carbon (mg) left after the CBD extraction,

$TOC_{control}$ = total organic carbon (mg) left after the control extraction,

$fTOC_{CBD} = TOC_{CBD}/TOC_{control}$,

$fFe_R\text{-}OC = Fe_R\text{-}OC/TOC_{control}$,

$\delta^{13}C_{CBD}$ = the measured carbon isotope signature of TOC_{CBD},

$\delta^{13}C_{control}$ = the measured carbon isotope signature of $TOC_{control}$,

$\delta^{13}C_{FeR\text{-}OC}$ = the carbon isotope signature of Fe_R-OC.

Geochemical modeling

Net reaction rates of sulfate were estimated using the MATLAB (2021b) script published in Wang et al.[65], considering molecular diffusion, sediment burial, fluid advection, and reaction under the assumption that the sulfate concentration profiles represent steady-state conditions.

The mass balance of sulfate is expressed as:

$$-\frac{\partial}{\partial x}\left\{-\frac{D(x)}{\theta^2(x)}\frac{\partial[\varnothing(x)C(x)]}{\partial x}+\left[\varnothing(x)b(x)+\varnothing(x)\upsilon(x)\right]C(x)\right\}+R(x)=0 \tag{4}$$

Where $C(x)$ is sulfate concentration in the porewater, x is depth below the seafloor, $\varnothing(x)$ is porosity, $D(x)$ is the molecular diffusion coefficient of sulfate, $\theta^2(x)$ is tortuosity, $b(x)$ is porewater burial velocity, $\upsilon(x)$ is externally driven flow velocity, $R(x)$ is the rate of diagenetic reaction per unit volume of sediment[65].

The model applied a 5-point Gaussian filter to the sulfate concentration profile, with the weighting on the 5 points of: [0.06, 0.24, 0.4, 0.24, 0.06]. All parameters used for modeling are listed in Supplementary Table 2. Porosity profile was measured using QDN-G1 samples. The averaged porosity was applied as the constant porosity value for both cores assuming similar sediment properties in the study area. Diffusion coefficients of sulfate in the two cores were obtained using R package marelac[66] with the input of respective salinity, temperature and pressure values (Supplementary Table 2). The tortuosity θ^2 was calculated by the relation, $\theta^2 = \varnothing f$, where f is the formation factor, which can be calculated based on the empirical relationship $f = 1.3 \times \varnothing^{-1.45}$[67,68]. We used the sedimentation rate near the seafloor 1.2×10^{-4} m yr^{-1} as the porewater burial velocity for both cores, assuming a similar sedimentation rate in the study area, which is calculated by the radiocarbon dating ages of the first two sampling layers below the seafloor in QDN-G1. A constant external flow advection velocity near the sediment-water interface of 10^{-5} m yr^{-1} was used[65]. A minimum of three measured concentration data points were used to determine each reaction zone[65]. The model quantifies uncertainties in the rate estimates by using a Monte Carlo technique[65]. The depth-integrated net reaction rate yielded the total flux at steady state for the sediment column.

Estimation of TOC and Fe_R-OC remineralization fluxes in the SMTZ

The remineralization fluxes of TOC and Fe_R-OC in the SMTZ can be estimated by the difference of their average accumulation rates between the sediment column above and within the SMTZ, assuming that all the TOC and Fe_R-OC lost in the SMTZ is remineralized by heterotrophic microorganisms as opposed to mobilized and moved into another organic carbon pool.

The accumulation rates of TOC and Fe_R-OC are calculated by multiplying their contents in sediments by the sediment mass accumulation rate[69]:

$$\text{TOC accumulation rate} = \text{LSR} \times \text{DBD} \times \text{TOC\%} \tag{5}$$

$$\text{Fe}_\text{R}\text{-OC accumulation rate} = \text{LSR} \times \text{DBD} \times \text{Fe}_\text{R} - \text{OC\%} \tag{6}$$

where DBD is the dry sediment bulk density in g cm^{-3}, LSR is the linear sedimentation rate in cm kyr^{-1}, TOC% and Fe_R-OC% are the weight percentage of TOC and Fe_R-OC in sediments, respectively. The TOC and Fe_R-OC accumulation rates are expressed in mol m^{-2} kyr^{-1}. The average sedimentation rate (11.1 cm kyr^{-1}) and the average dry bulk density (0.9 g cm^{-3}) of QDN-G1 was used for the calculation for core QDN-14B, assuming similar sedimentation rate and bulk sediment properties in the study area.

When assigning the background levels of TOC and Fe_R-OC accumulation rates, which are independent of remineralization within the SMTZ, the average accumulation rate in the sediment column above the SMTZ was used. As TOC and Fe_R-OC contents in core QDN-G1 begin to steadily decline above the SMTZ (Fig. 2b), this approach may lead to an overestimation of remineralization fluxes within the SMTZ. Therefore, for core QDN-G1, we estimated a lower boundary of background TOC and Fe_R-OC accumulation rates, represented by the four samples above the SMTZ (560–720 cmbsf) as average.

DNA extraction, qPCR and amplicon sequencing

The 16 S rRNA gene data was obtained for core QDN-G1 according to the following procedures.

The DNA for qPCR and V4 region of 16 S rRNA gene sequencing was extracted from ~0.25 g of sediments using DNeasy® PowerSoil® Pro Kit (Cat. No. 47014, Qiagen, Germany), according to the manufacturer's instructions.

The extracted DNA was used as template for qPCR to determine the abundance of bacterial 16 S rRNA gene with the primer set 331 F (5′-TCCTACGGGAGGCAGCAGT-3′) /797 R (5′-GGACTACCAGGGTATCTAATCCTGTT-3′)[70]. Standard curves were constructed using a 10-fold series dilution of the plasmids for six gradients carrying the bacteria 16 S rRNA gene. qPCR was carried out in a volume of 20 μL, including 10 μL 2 × PowerUp™ SYBR™ Green Master Mix (Cat. No. A25742, Thermo Scientific, USA), 1.6 μL each primer (10 μM), 2 μL template DNA and 4.8 μL steriled deionized water. The qPCR program consisted of an initial cycle of 95 °C for 5 min; 40 cycles of 95 °C for 30 s, 60 °C for 30 s, 72 °C for 30 s, 80 °C for 10 s, and the data was collected at the final step of each cycle. The melting curve was generated using default program. All samples were subject to qPCR measurement with three technical replicates. The bacterial cell number was evaluated based on the abundance of 16 S rRNA gene, applying the average copy number of the 16 S rRNA gene on genomes of Bacteria (5.3 copies/genome, rrnDB version 5.8)[71].

The V4 region of 16 S rRNA gene was amplified using the primer set 515 F (5′-GTGYCAGCMGCCGCGGTAA-3′) /806 R (5′-GGACTACNVGGGTWTCTAAT-3′)[72]. DNA was amplified using the following cycling conditions: 95 °C, 5 min; 30 cycles (95 °C, 30 s; 50 °C, 30 s; 72 °C, 30 s); 72 °C, 7 min. The PCR products of samples were sent to Shanghai Personal Biotechnology Co., Ltd. (Shanghai, China) for high-throughput sequencing of the 16 S rRNA gene using the Illumina Novaseq PE250 platform.

Sequence analysis

The raw reads of 16 S rRNA gene of both cores QDN-G1 and QDN-14B were processed and analyzed using the QIIME 2 platform (version 2020.11)[73]. The primers and adapters were first trimmed out using Cutadapt (version 3.1)[74]. Raw sequences were then processed using DADA2[75], including quality filtering, denoising, paired-end sequence merging, chimera filtering and producing amplicon sequence variants (ASVs) and ASV Table. Taxonomy was assigned using q2-feature-classifier (a scikit-learn naive Bayes machine-learning classifier)[76] with Silva database release 138[77]. Multiple sequence alignment and phylogenetic tree construction were performed using the QIIME 2 plugin q2-phylogeny (align-to-tree-mafft-iqtree). Unassigned sequences, singletions and sequences affiliated with eukaryotes were discarded. Eventually, to eliminate uneven sequencing depths, the ASV table was rarefied to 14935 and 71773 sequences per sample for QDN-14B and QDN-G1, respectively, determined by the sample with the fewest sequences (Supplementary Data 1 and 2).

Statistical analyzes

Statistical analyzes were carried out in R (version 4.1.3). The Wilcoxon rank sum test was applied to compare TOC and Fe_R-OC records between SMTZ and non-SMTZ sediments in two sediment cores studied, including TOC content, Fe_R-OC content, fFe_R-OC, $\delta^{13}C_{TOC}$, and $\delta^{13}C_{FeR\text{-}OC}$.

One-way analysis of variance (ANOVA) was used to determine if there are significant differences in fFe_R-OC in surface sediments of different marine environments. Tukey Honest Significant Difference (HSD) test was used for performing multiple pairwise-comparison between the environments to determine which among them were significantly different.

Reporting summary

Further information on research design is available in the Nature Portfolio Reporting Summary linked to this article.

Data availability

Raw Illumina sequence data of the 16 S rRNA gene generated for cores QDN-14B and QDN-G1 in this study have been deposited in the National Omics Data Encyclopedia (NODE, https://www.biosino.org/node/) database under the project number OEP004264 and OEP004265, as well as the NCBI SRA database under the BioProject IDs of PRJNA1130026 and PRJNA1129281. All other data discussed in the paper are available in the paper or in the Supplementary Data. All the data files are available in the Figshare database (https://doi.org/10.6084/m9.figshare.26155303). Source data are provided with this paper.

References

1. Berner, R. A. GEOCARBSULF: A combined model for phanerozoic atmospheric O_2 and CO_2. *Geochim. Cosmochim. Acta* **70**, 5653–5664 (2006).
2. Lalonde, K., Mucci, A., Ouellet, A. & Gélinas, Y. Preservation of organic matter in sediments promoted by iron. *Nature* **483**, 198–200 (2012).
3. Salvadó, J. A. et al. Organic carbon remobilized from thawing permafrost is resequestered by reactive iron on the Eurasian Arctic Shelf. *Geophys. Res. Lett.* **42**, 8122–8130 (2015).
4. Barber, A. et al. Preservation of organic matter in marine sediments by inner-sphere interactions with reactive iron. *Sci. Rep.* **7**, 366 (2017).
5. Kaiser, K. & Guggenberger, G. The role of DOM sorption to mineral surfaces in the preservation of organic matter in soils. *Org. Geochem.* **31**, 711–725 (2000).
6. Mikutta, R., Kleber, M., Torn, M. S. & Jahn, R. Stabilization of soil organic matter: association with minerals or chemical recalcitrance? *Biogeochemistry* **77**, 25–56 (2006).
7. Jones, D. & Edwards, A. Influence of sorption on the biological utilization of two simple carbon substrates. *Soil Biol. Biochem.* **30**, 1895–1902 (1998).
8. Eusterhues, K., Neidhardt, J., Hädrich, A., Küsel, K. & Totsche, K. U. Biodegradation of ferrihydrite-associated organic matter. *Biogeochemistry* **119**, 45–50 (2014).
9. Longman, J., Faust, J. C., Bryce, C., Homoky, W. B. & März, C. Organic carbon burial with reactive iron across global environments. *Glob. Biogeochemical Cycles* **36**, e2022GB007447 (2022).
10. Friedlingstein, P. et al. Global Carbon Budget 2023. *Earth Syst. Sci. Data* **15**, 5301–5369 (2023).
11. Longman, J., Gernon, T. M., Palmer, M. R. & Manners, H. R. Tephra deposition and bonding with reactive oxides enhances burial of organic carbon in the Bering Sea. *Glob. Biogeochemical Cycles* **35**, e2021GB007140 (2021).
12. Longman, J. et al. Production and preservation of organic carbon in sub-seafloor tephra layers. *Mar. Chem.* **258**, 104334 (2024).
13. Faust, J. C. et al. Millennial scale persistence of organic carbon bound to iron in Arctic marine sediments. *Nat. Commun.* **12**, 275 (2021).
14. Sun, C.-H. et al. Examining bulk and iron-associated organic carbon through depth in margin sea sediments (China) under contrasting depositional settings: Chemical and NEXAFS spectral characterization. *J. Mar. Syst.* **207**, 103344 (2020).
15. Wagai, R. & Mayer, L. M. Sorptive stabilization of organic matter in soils by hydrous iron oxides. *Geochim. Cosmochim. Acta* **71**, 25–35 (2007).
16. Wang, S. et al. Potential retention of dissolved organic matter by soil minerals during wetland water-table fluctuations. *Water Res.* **254**, 121412 (2024).
17. Chen, C. & Coward, E. Iron-mediated organic matter decomposition in humid soils can counteract protection. *Nat. Commun.* **11**, 2255 (2020).
18. Patzner, M. S. et al. Iron mineral dissolution releases iron and associated organic carbon during permafrost thaw. *Nat. Commun.* **11**, 6329 (2020).
19. Melton, E. D., Swanner, E. D., Behrens, S., Schmidt, C. & Kappler, A. The interplay of microbially mediated and abiotic reactions in the biogeochemical Fe cycle. *Nat. Rev. Microbiol.* **12**, 797–808 (2014).
20. Liang, L., Wang, Y., Sivan, O. & Wang, F. Metal-dependent anaerobic methane oxidation in marine sediment: Insights from marine settings and other systems. *Sci. China Life Sci.* **62**, 1287–1295 (2019).
21. Liang, L. et al. Iron (oxyhydr)oxides shift the methanogenic community in deep sea methanic sediment - insights from long-term high-pressure incubations. *Sci. Total Environ.* **848**, 157590 (2022).
22. Adhikari, D. et al. Asynchronous reductive release of iron and organic carbon from hematite–humic acid complexes. *Chem. Geol.* **430**, 13–20 (2016).
23. Zhao, Q. et al. Coupled dynamics of iron and iron-bound organic carbon in forest soils during anaerobic reduction. *Chem. Geol.* **464**, 118–126 (2017).
24. Zeng, Q. et al. Bio-reduction of ferrihydrite-montmorillonite-organic matter complexes: Effect of montmorillonite and fate of organic matter. *Geochim. Cosmochim. Acta* **276**, 327–344 (2020).
25. Cartapanis, O., Bianchi, D., Jaccard, S. L. & Galbraith, E. D. Global pulses of organic carbon burial in deep-sea sediments during glacial maxima. *Nat. Commun.* **7**, 10796 (2016).
26. He, J., Zhao, M., Li, L., Wang, P. & Ge, H. Sea surface temperature and terrestrial biomarker records of the last 260 ka of core MD05-2904 from the northern South China Sea. *Chin. Sci. Bull.* **53**, 2376–2384 (2008).
27. Poulton, S. & Raiswell, R. The low-temperature geochemical cycle of iron: from continental fluxes to marine sediment deposition. *Am. J. Sci.* **302**, 774–805 (2002).
28. Niu, M., Fan, X., Zhuang, G., Liang, Q. & Wang, F. Methane-metabolizing microbial communities in sediments of the Haima cold seep area, northwest slope of the South China Sea. *FEMS Microbiol. Ecol.* **93**, fix101 (2017).
29. Mehra, O. & Jackson, M. Iron oxide removal from soils and clays by a dithionite-citrate system buffered with sodium bicarbonate. *Clays Clay Miner.* **7**, 317–327 (1960).
30. Canfield, D. E. & Thamdrup, B. Towards a consistent classification scheme for geochemical environments, or, why we wish the term 'suboxic'would go away. *Geobiology* **7**, 385–392 (2009).
31. He, B. et al. Sources and accumulation of organic carbon in the Pearl River Estuary surface sediment as indicated by elemental, stable carbon isotopic, and carbohydrate compositions. *Biogeosciences* **7**, 3343–3362 (2010).
32. Wei, B., Mollenhauer, G., Hefter, J., Grotheer, H. & Jia, G. Dispersal and aging of terrigenous organic matter in the Pearl River Estuary and the northern South China Sea Shelf. *Geochim. Cosmochim. Acta* **282**, 324–339 (2020).
33. Wang, X.-C., Druffel, E. R., Griffin, S., Lee, C. & Kashgarian, M. Radiocarbon studies of organic compound classes in plankton and sediment of the northeastern Pacific Ocean. *Geochim. Cosmochim. Acta* **62**, 1365–1378 (1998).
34. Yang, S. et al. Genomic and enzymatic evidence of acetogenesis by anaerobic methanotrophic archaea. *Nat. Commun.* **11**, 3941 (2020).
35. Kaiser, K. & Guggenberger, G. Sorptive stabilization of organic matter by microporous goethite: sorption into small pores vs. surface complexation. *Eur. J. Soil Sci.* **58**, 45–59 (2007).

36. Contreras, S. et al. Cyclic 100-ka (glacial-interglacial) migration of subseafloor redox zonation on the Peruvian shelf. *Proc. Natl Acad. Sci.* **110**, 18098–18103 (2013).
37. Riedinger, N. et al. Diagenetic alteration of magnetic signals by anaerobic oxidation of methane related to a change in sedimentation rate. *Geochim. Cosmochim. Acta* **69**, 4117–4126 (2005).
38. Yoshinaga, M. Y. et al. Carbon isotope equilibration during sulphate-limited anaerobic oxidation of methane. *Nat. Geosci.* **7**, 190–194 (2014).
39. Boetius, A. et al. A marine microbial consortium apparently mediating anaerobic oxidation of methane. *Nature* **407**, 623–626 (2000).
40. Wang, Y., Wegener, G., Ruff, S. E. & Wang, F. Methyl/alkyl-coenzyme M reductase-based anaerobic alkane oxidation in archaea. *Environ. Microbiol.* **23**, 530–541 (2021).
41. Dos Santos Afonso, M. & Stumm, W. Reductive dissolution of iron(III) (hydr)oxides by hydrogen sulfide. *Langmuir* **8**, 1671–1675 (1992).
42. Canfield, D. E., Raiswell, R. & Bottrell, S. H. The reactivity of sedimentary iron minerals toward sulfide. *Am. J. Sci.* **292**, 659–683 (1992).
43. Lovley, D. R., Roden, E. E., Phillips, E. J. P. & Woodward, J. C. Enzymatic iron and uranium reduction by sulfate-reducing bacteria. *Mar. Geol.* **113**, 41–53 (1993).
44. Li, Y.-L., Vali, H., Yang, J., Phelps, T. J. & Zhang, C. L. Reduction of iron oxides enhanced by a sulfate-reducing bacterium and biogenic H_2S. *Geomicrobiol. J.* **23**, 103–117 (2006).
45. Cai, C. et al. A methanotrophic archaeon couples anaerobic oxidation of methane to Fe(III) reduction. *ISME J.* **12**, 1929–1939 (2018).
46. Egger, M., Riedinger, N., Mogollón, J. M. & Jørgensen, B. B. Global diffusive fluxes of methane in marine sediments. *Nat. Geosci.* **11**, 421–425 (2018).
47. Hedges, J. I. & Keil, R. G. Sedimentary organic matter preservation: an assessment and speculative synthesis. *Mar. Chem.* **49**, 81–115 (1995).
48. LaRowe, D. E. et al. Organic carbon and microbial activity in marine sediments on a global scale throughout the Quaternary. *Geochim. Cosmochim. Acta* **286**, 227–247 (2020).
49. Bradley, J. Sources and fluxes of organic carbon and energy to microorganisms in global marine sediments. *Front. Microbiol.* **13**, 910694 (2022).
50. Kallmeyer, J., Pockalny, R., Adhikari, R. R., Smith, D. C. & D'Hondt, S. Global distribution of microbial abundance and biomass in subseafloor sediment. *Proc. Natl Acad. Sci.* **109**, 16213–16216 (2012).
51. Jickells, T. et al. Global iron connections between desert dust, ocean biogeochemistry, and climate. *Science* **308**, 67–71 (2005).
52. Shields, M. R., Bianchi, T. S., Gélinas, Y., Allison, M. A. & Twilley, R. R. Enhanced terrestrial carbon preservation promoted by reactive iron in deltaic sediments. *Geophys. Res. Lett.* **43**, 1149–1157 (2016).
53. Zhao, B. et al. The role of reactive iron in the preservation of terrestrial organic carbon in estuarine sediments. *J. Geophys. Res. Biogeosci.* **123**, https://doi.org/10.1029/2018JG004649 (2018).
54. Zhao, B. et al. Preferential preservation of pre-aged terrestrial organic carbon by reactive iron in estuarine particles and coastal sediments of a large river-dominated estuary. *Geochim. Cosmochim. Acta* **345**, 34–49 (2023).
55. Wagner, S. et al. Soothsaying DOM: A current perspective on the future of oceanic dissolved organic carbon. *Front. Mar. Sci.* **7**, 341 (2020).
56. Kleber, M. et al. Dynamic interactions at the mineral–organic matter interface. *Nature Reviews Earth & Environment*, 1-20 (2021).
57. Riedel, T., Zak, D., Biester, H. & Dittmar, T. Iron traps terrestrially derived dissolved organic matter at redox interfaces. *Proc. Natl Acad. Sci.* **110**, 10101–10105 (2013).
58. Zhao, Z. et al. The high resolution sedimentary filling in Qiongdongnan Basin, Northern South China Sea. *Mar. Geol.* **361**, 11–24 (2015).
59. Liu, X. et al. A heavy mineral viewpoint on sediment provenance and environment in the Qiongdongnan Basin. *Acta Oceanologica Sin.* **34**, 41–55 (2015).
60. Hu, Y. et al. Pore fluid compositions and inferred fluid flow patterns at the Haima cold seeps of the South China Sea. *Mar. Pet. Geol.* **103**, 29–40 (2019).
61. Lisiecki, L. E. & Raymo, M. E. A Pliocene-Pleistocene stack of 57 globally distributed benthic $\delta^{18}O$ records. *Paleoceanography* **20**, PA1003 (2005).
62. Stookey, L. L. Ferrozine–a new spectrophotometric reagent for iron. *Anal. Chem.* **42**, 779–781 (1970).
63. van der Zee, C., Roberts, D. R., Rancourt, D. G. & Slomp, C. P. Nanogoethite is the dominant reactive oxyhydroxide phase in lake and marine sediments. *Geology* **31**, 993–996 (2003).
64. Zhang, Y. G., Ji, J., Balsam, W. L., Liu, L. & Chen, J. High resolution hematite and goethite records from ODP 1143, South China Sea: Co-evolution of monsoonal precipitation and El Niño over the past 600,000 years. *Earth Planet. Sci. Lett.* **264**, 136–150 (2007).
65. Wang, G., Spivack, A. J., Rutherford, S., Manor, U. & D'Hondt, S. Quantification of co-occurring reaction rates in deep subseafloor sediments. *Geochim. Cosmochim. Acta* **72**, 3479–3488 (2008).
66. Soetaert, K., Petzoldt, T. & Meysman, F. marelac: Tools for aquatic sciences. R package version 2.1 http://CRAN.R-project.org/package=marelac (2010).
67. Boyce, R. E. Electrical resistivity of modern marine sediments from the Bering Sea. *J. Geophys. Res.* **73**, 4759–4766 (1968).
68. Breitzke, M. Physical Properties of Marine Sediments. In: *Marine Geochemistry* (eds Schulz H. D., Zabel M.). Springer Berlin Heidelberg (2006).
69. Xu, Y. et al. Distribution, source, and burial of sedimentary organic carbon in kermadec and atacama trenches. *J. Geophys. Res. Biogeosci.* **126**, e2020JG006189 (2021).
70. Santelli, C. M. et al. Abundance and diversity of microbial life in ocean crust. *Nature* **453**, 653–656 (2008).
71. Stoddard, S. F., Smith, B. J., Hein, R., Roller, B. R. K. & Schmidt, T. M. rrnDB: improved tools for interpreting rRNA gene abundance in bacteria and archaea and a new foundation for future development. *Nucleic Acids Res.* **43**, D593–D598 (2014).
72. Caporaso, J. G. et al. Global patterns of 16S rRNA diversity at a depth of millions of sequences per sample. *Proc. Natl Acad. Sci.* **108**, 4516–4522 (2011).
73. Bolyen, E. et al. Reproducible, interactive, scalable and extensible microbiome data science using QIIME 2. *Nat. Biotechnol.* **37**, 852–857 (2019).
74. Martin, M. Cutadapt removes adapter sequences from high-throughput sequencing reads. *EMBnet. J.* **17**, 10–12 (2011).
75. Callahan, B. J. et al. DADA2: high-resolution sample inference from Illumina amplicon data. *Nat. Methods* **13**, 581–583 (2016).
76. Bokulich, N. A. et al. Optimizing taxonomic classification of marker-gene amplicon sequences with QIIME 2's q2-feature-classifier plugin. *Microbiome* **6**, 1–17 (2018).
77. Quast, C. et al. The SILVA ribosomal RNA gene database project: improved data processing and web-based tools. *Nucleic Acids Res.* **41**, D590–D596 (2012).
78. Müller, A. L., Kjeldsen, K. U., Rattei, T., Pester, M. & Loy, A. Phylogenetic and environmental diversity of DsrAB-type dissimilatory (bi) sulfite reductases. *ISME J.* **9**, 1152–1165 (2015).

Acknowledgements

We thank the crew members of the R/V Haiyang IV cruise '20150402' and the R/V KEXUE cruise 'Hydrothermal vents-cold seeps' for sample collection. We would like to express our gratitude to Shanshan Zhang, Dr. Li Zhang and Dr. Fan Yang for their help with the EA-IRMS measurement at the instrumental analysis center, Shanghai Jiao Tong

University. This work was supported by the National Natural Science Foundation of China (NSFC grant No. 42230401, 92251303 to FW, and 42006083 to MN) and by the Deutsche Forschungsgemeinschaft via Germany's Excellence Strategy, no. EXC-2077-390741603 (to YC and KUH). This is also a contribution to the "2030" program of Shanghai Jiao Tong University (WH510244001) (to FW) and supported by the project "Ocean Negative Carbon Emission (ONCE)".

Author contributions

F.W., Y.C. and L.D. designed the research. Y.C. collected geochemical data and performed data analysis. L.D. constructed the age model. W.S. and M.N. collected microbial data and performed data analysis. Y.C. wrote the first draft of the manuscript. Y.C. and F.W. finished the manuscript with substantial contributions from L.D., X.C. and K.-U.H. All coauthors contributed to the interpretation of the results and commented on the manuscript.

Competing interests

The authors declare no competing interests.

Additional information

Supplementary information The online version contains supplementary material available at https://doi.org/10.1038/s41467-024-50578-5.

Correspondence and requests for materials should be addressed to Fengping Wang.

Peer review information *Nature Communications* thanks Guizhi Wang, Limin Hu and Jack Longman for their contribution to the peer review of this work. A peer review file is available.